

On the Controllability and Observability of Temperature States in Metal Powder Bed Fusion

Nathaniel Wood¹

Mem. ASME
Department of Mechanical and
Aerospace Engineering,
Ohio State University,
Columbus, OH 43210
e-mail: wood.863@osu.edu

David J. Hoelzle

Mem. ASME
Department of Mechanical and
Aerospace Engineering,
Ohio State University,
Columbus, OH 43210
e-mail: hoelzle.1@osu.edu

Powder bed fusion (PBF) is an additive manufacturing (AM) process that builds parts in a layer-by-layer fashion out of a bed of metal powder via the selective melting action of a laser or electron beam heat source. Despite its transformational manufacturing capabilities, PBF is currently controlled in the open loop and there is significant demand to apply closed-loop process monitoring and control to the thermal management problem. This paper introduces a controls theoretic analysis of the controllability and observability of temperature states in PBF. The main contributions of the paper are proofs that certain configurations of PBF are classically controllable and observable, but that these configurations are not strongly structurally controllable and observable. These results are complemented by case studies, demonstrating the energy requirement of state estimation under various, industry relevant PBF configurations. These fundamental characterizations of controllability and observability provide a basis for realizing closed-loop PBF temperature estimation. [DOI: 10.1115/1.4056326]

1 Introduction

Powder bed fusion (PBF) is a class of additive manufacturing (AM) processes. Commonly referred to as "three-dimensional (3D) printing," AM processes have rapidly grown in popularity and market size because they can produce geometrically complex parts with engineering properties similar to those produced by conventional manufacturing processes while removing much of the overhead costs of production [1,2]. Although PBF can utilize metallic, polymeric, and ceramic feedstocks, the contributions of this paper are relevant to metallic feedstocks and their associated thermomechanical properties. The PBF process (Fig. 1) builds three-dimensional parts out of layers of powder, using a build cycle of (1) sweeping a thin layer of powder over the machine base plate or previously fused powder, (2) selectively melting a 2D pattern of desired geometry into the powder with a highpowered laser or electron beam (e-beam), and (3) lowering the base plate in the—z direction to accommodate a new layer of powder.

Powder bed fusion is not without flaws. It is well-documented that parts manufactured by PBF may suffer from high levels of residual stresses [5,6], porosity [7,8], and anisotropy in material properties [2,9–11], and that these defects arise from poor thermal management of the PBF process during production. Although PBF thermal management is critical for producing high-quality parts, temperatures are typically controlled in the open loop, making no use of available sensor data. The energy irradiated to the powder, *u*, is specified by a schedule directed by computer numerical control language [12]. Assignment of schedule parameters is determined in advance through operator experience, heuristically through design-of-experiment procedures [13], and/or with computationally complex predictive models [14]. Monitoring the thermal profile during production with infrared sensors remains a

challenge. Parts are typically checked for defects and compliance with specifications after the build is complete, potentially incurring substantial losses in time, money, and materials. Significant advances in PBF production quality could be achieved with in situ process monitoring and control of the thermal management problem [15,16]. Despite the need for PBF thermal management, the community has not yet evaluated the basic criteria for the feasibility of designing process monitoring and control algorithms: the requirement that the process is observable and controllable. This paper answers this basic question. Our analysis takes an aspirational approach. (1) We consider both current and emerging thermal actuation and sensing hardware capabilities to ensure that the theory is developed for current and future PBF practice. (2) Computational requirements are not considered here. Although important, the complex domains of PBF are best analyzed by spatially discretizing the domain, which leads to large systems. We anticipate computational burdens to ease with advancing computer power. We also anticipate that the controls theoretic properties of these large models will be a foundation for assessing the same properties of more sophisticated, computationally efficient models in future studies. This provides a framework to apply modern control and estimation tools such as state estimators and fault detection schemes to the process monitoring problem, and advanced control strategies like multivariable robust controllers and model predictive control.

The intended audiences for this paper are additive manufacturing researchers who are interested in PBF process monitoring applications and control systems researchers who are interested in the PBF application. To communicate with the intended audiences, this paper translates established control and network theory for system models of PBF. Section 2 defines controllability and observability in the context of PBF, provides an overview of the established systems and network theory that are leveraged in this work, and provides an overview of the PBF thermal physics and hardware configurations under consideration. Section 3 constructs a set of linear systems from these thermal physics and hardware configurations. Section 4 derives conditions under which the resultant linear systems are controllable and observable, as

¹Corresponding author.

Contributed by the Dynamic Systems Division of ASME for publication in the JOURNAL OF DYNAMIC SYSTEMS, MEASUREMENT, AND CONTROL. Manuscript received October 9, 2021; final manuscript received November 16, 2022; published online December 23, 2022. Assoc. Editor: Sandipan Mishra.

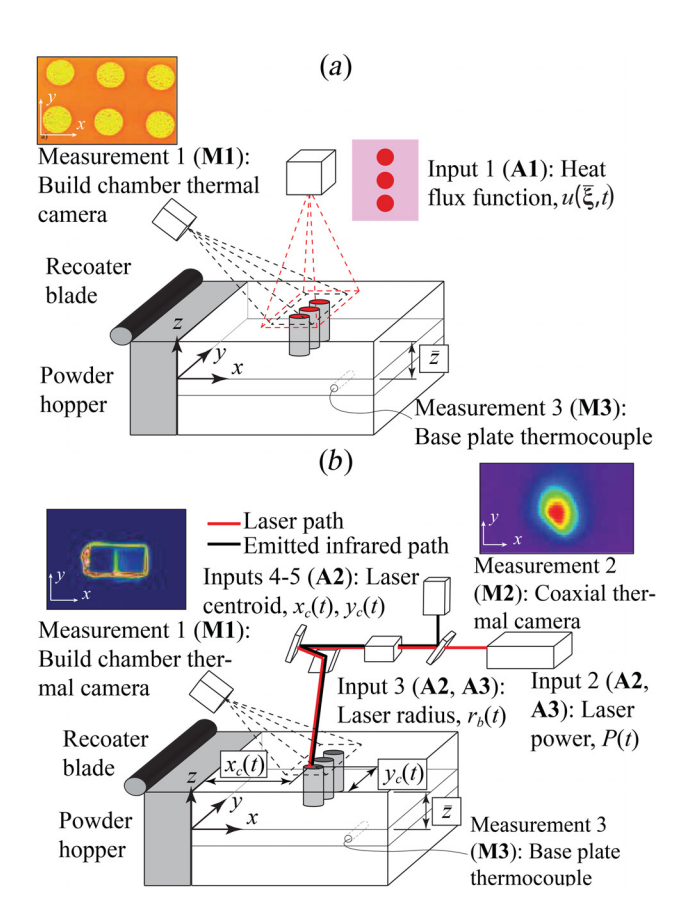


Fig. 1 System schematics of powder bed fusion (PBF) additive manufacturing. Reproduced from Wood et al. [3] with permission from IEEE. Bolded abbreviations A1-A3 and M1-M3 denote actuation and measurement modes described in Appendix A. (a) Input and output channels for E-PBF and PBF with a digital light processing filter. The example Measurement 1 image is reproduced from Ridwan et al. [4] with permission from The Minerals, Metals, and Materials Society. (b) Input and output channels for standard L-PBF and E-PBF with a slow raster speed.

constructed from different actuation and measurement modes, as well as showing examples of part geometries that are controllable and observable. However, controllability and observability as defined in Sec. 2 are binary metrics. We demonstrate energetic considerations of state observation in Sec. 5, where we show the energy required to estimate certain temperature states. Section 6 presents our conclusions.

2 Preliminaries

Throughout this paper, we will denote scalar variables and functions by italicized variables and vector-valued functions as bold-face variables. For example, T is the 3D part temperature function whereas \mathbf{x} is a vector of temperatures at discretized nodes. \mathbf{I}_m is the $m \times m$ identity matrix, $\mathbf{0}_{n \times m}$ is the $n \times m$ zero matrix.

We leverage concepts of controllability, observability, strong structural controllability, and strong structural observability for linear time-varying (LTV) systems of the form (1), and linear time-invariant (LTI) systems of the form (2). Here, $\mathbf{x}(t) \in \mathbb{R}^n$ (discretized internal temperature field) is the state vector. $\mathbf{u}(t) \in \mathbb{R}^m$ is the input vector, and $\mathbf{y}(t) \in \mathbb{R}^p$ is the output vector, both of which are to be defined. \mathbf{A} , $\mathbf{B}(t)$, and $\mathbf{C}(t)$ have appropriate dimensions

$$\dot{\mathbf{x}}(t) = \mathbf{A}\mathbf{x}(t) + \mathbf{B}(t)\mathbf{u}(t)$$

$$\mathbf{y}(t) = \mathbf{C}(t)\mathbf{x}(t)$$
(1)

$$\dot{\mathbf{x}}(t) = \mathbf{A}\mathbf{x}(t) + \mathbf{B}\mathbf{u}(t)$$
$$\mathbf{y}(t) = \mathbf{C}\mathbf{x}(t)$$
 (2)

2.1 Controllability and Observability Criteria. The following are standard textbook definitions from Refs. [17] and [18]; the intention is to develop a set of preliminaries to reference throughout the paper. The criteria for controllability and observability are built from the definition of the state transition matrix, $\Phi(t, t_0)$, which describes the mapping from the initial state $\mathbf{x}(t_0)$ and input function $\mathbf{u}(t)$ to the state at time t, $\mathbf{x}(t)$

$$\mathbf{x}(t) = \mathbf{\Phi}(t, t_0)\mathbf{x}_0 + \int_{t_0}^t \mathbf{\Phi}(t, \tau)\mathbf{B}(\tau)\mathbf{u}(\tau)d\tau$$
 (3)

In the context of PBF, $\Phi(t, t_0)$ captures the internal dynamics that relate an initial temperature field to the temperature field at time t. An input $\mathbf{u}(t)$ can be constructed to drive the system from $\mathbf{x}(t_0)$ to any $\mathbf{x}(t_1)$, thus the system is (completely) controllable, if and only if the controllability Gramian

$$\mathbf{W}_c(t_0, t_1) = \int_{t_0}^{t_1} \mathbf{\Phi}(t_1, \tau) \mathbf{B}(\tau) \mathbf{B}'(\tau) \mathbf{\Phi}'(t_1, \tau) d\tau \tag{4}$$

is nonsingular. $[\cdot]'$ denotes the transpose operator. Analogously, any initial state $\mathbf{x}(t_0)$ can be reconstructed from knowledge of the input $\mathbf{u}(t)$ and output $\mathbf{y}(t)$, thus the system is observable, if and only if the observability Gramian

$$\mathbf{W}_o(t_0, t_1) = \int_{t_0}^{t_1} \mathbf{\Phi}'(t_1, \tau) \mathbf{C}'(\tau) \mathbf{C}(\tau) \mathbf{\Phi}(t_1, \tau) d\tau$$
 (5)

is nonsingular.

In the context of PBF, (complete) controllability means there always exists an actuation function, $\mathbf{u}(t)$, that causes the temperature field in the part, $\mathbf{x}(t)$, to track the desired trajectory. In practice, this means that the temperature field inside the part can be sculpted in time. Observability means that we can estimate the temperature field history solely from knowledge of the actuation function $\mathbf{u}(t)$ and the measurement function $\mathbf{y}(t)$.

2.2 Strong Structural Controllability and Observability.

To bound our controllability and observability analysis, we use the concepts of strong structural controllability (SSC) and strong structural observability (SSO). Using graph network theory, these properties assess if certain system parameter combinations exist which produce an uncontrollable or unobservable system, respectively. For PBF, these parameters include geometric features, material properties, and actuation design. We use the definition of SSC given in Ref. [19]:

Definition 1. The system $(\mathbf{A}_0,\,\mathbf{B}_0)$ is SSC if any system $(\mathbf{A}_1,\,\mathbf{B}_1)$ which has the same structure as $(\mathbf{A}_0,\,\mathbf{B}_0)$ is completely controllable as long as every free parameter of the matrix $[\mathbf{A}_1,\,\mathbf{B}_1]$ is nonzero.

Here, the *structure* of the pair (A_0, B_0) is the location of all nonzero entries of the matrices A_0 and B_0 , which are described as "free parameters" in Definition 1. A similar criterion exists for SSO [20]. Systems that are SSC (SSO) will be controllable or observable in the sense of Sec. 2.1 regardless of any variations in nonzero matrix entries. Assessing SSC and SSO requires analyzing the system as a graph. We introduce this topic using the notation of Ref. [21], which readers should consult for more detail.

Construction of the graph corresponding to Eq. (2), $G(\mathbf{A}, \mathbf{B}, \mathbf{C})$, is demonstrated in Fig. 2. The nodes of $G(\mathbf{A}, \mathbf{B}, \mathbf{C})$ are the components of $\mathbf{x}(t)$, $\mathbf{u}(t)$ (driver nodes), and $\mathbf{y}(t)$ (observer nodes). The nonzero entries of \mathbf{A} , \mathbf{B} , and \mathbf{C} determine which components of $\mathbf{x}(t)$ are connected by edges to other components of $\mathbf{x}(t)$, $\mathbf{u}(t)$, or

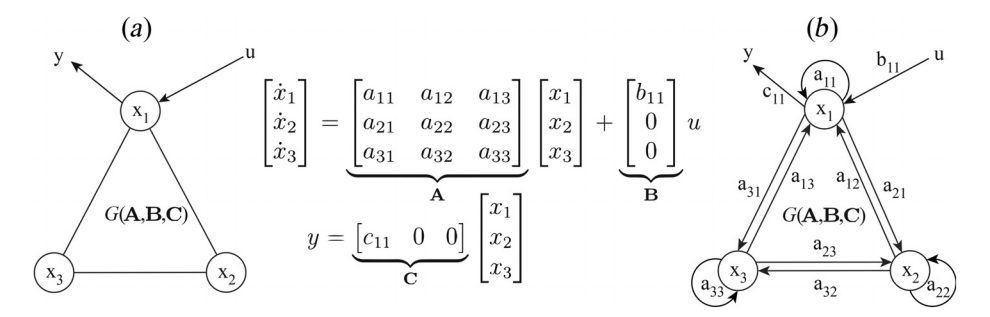


Fig. 2 Interpretation of an LTI system as a graph. (a) Simple model consisting of one element and three nodes with external input being applied to node 1 and a measurement taken of node 1. The A matrix maps heat flow. The B matrix maps the input u to the system nodes. The C matrix maps the state x to the output (measurement y). (b) Interpretation of the system as a directed network following the notation of Ref. [21], with edges of the network mapping heat flow between nodes according to the weights specified by A, B, and C.

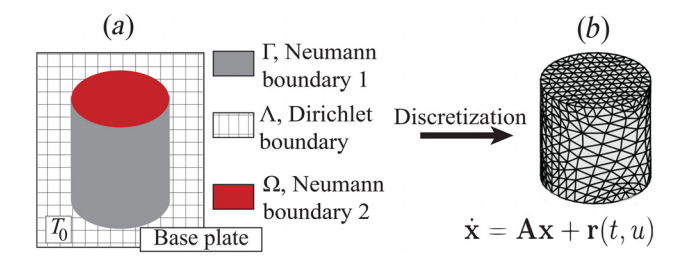


Fig. 3 Transition from a continuous model of PBF heat transfer to a FEM model: (a) description of PBF boundary conditions for a simple part and (b) FEM-based discretization of PBF solution domain and the associated system of coupled ODEs

 $\mathbf{y}(t)$, respectively, and the edge weights. Section 4 will show how the thermal models we derive in Sec. 3 relate to $G(\mathbf{A}, \mathbf{B}, \mathbf{C})$, although others have developed different graph theoretic representations of PBF for different analyses [22].

2.3 Powder Bed Fusion Actuation and Sensing Structure. We conclude these preliminaries with an overview of the existing and emerging PBF thermal physics and hardware configurations examined in this work. Consider a partially built part in a PBF system (Fig. 1). The part is the thermal domain, V, with heat transfer defined on the domain $\xi = \{x, y, z\} \in V \subset \mathbb{R}^3$ (Fig. 3(a)). V is bounded by the set of faces $S = \{\Lambda, \Gamma, \Omega\} \subset \mathbb{R}^3$, defined below:

- Λ contains all faces at the part bottom, consisting of points $\underline{\xi} = \{x, y, 0\} \in V$, which are in contact with the machine base plate.
- Ω contains all faces at the part top, consisting of points \(\bar{\xi} = \{x, y, \bar{z}\} \in V\), which are exposed to the environment, laser or e-beam energy sources, and vision-based thermal sensors.
- Γ contains all other bounding faces of the part. These faces are in contact with the surrounding metal powder.

Temperatures within V at coordinate ξ and time $t \ge 0$, denoted $T(\xi, t)$, are defined by the heat flux balance

$$\rho c \frac{dT(\xi, t)}{dt} = u(\bar{\xi}, t) - q_{\text{cond.}} - q_{\text{conv}} - q_{\text{rad}} - q_{\text{phase}}$$
 (6)

where $u(\bar{\xi},t)$ is the thermal energy delivered to the top face $\bar{\xi} \in \Omega$ from either laser or e-beam irradiation, $q_{\rm cond}$ is heat transfer via conduction, $q_{\rm conv}$ is heat transfer via convection, $q_{\rm rad}$ is heat transfer via radiation, $q_{\rm phase}$ is heat transfer associated with phase change, ρ is density and c is specific heat. As Fig. 3 demonstrates, we construct PBF models based on approximating the flux balance

(6) with the finite element method (FEM), which is common [23]. While other researchers have developed promising fast and accurate methods for solving (6) applied to PBF, we choose FEM for three reasons: (1) FEM has a lesser dependency on tunable hyperparameters and training data than graph theoretic methods [22] and machine learning models [24], respectively, (2) FEM more easily accommodates arbitrary geometry-imposed boundary conditions than Green's Function methods [25,26], and (3) FEM can model PBF dynamics at a higher resolution than path-level models [26,27], thus affording more sensitive process monitoring. As stated before, we anticipate the computational burden of FEM modeling to reduce with time, and for these results to be a foundation for assessing controls properties for more efficient models. Therefore, we consider a set of temperaures in V at the n nodes in our FEM mesh, $\xi_1, \xi_1, \ldots, \xi_n$, which is state vector $\mathbf{x}(t) \in \mathbb{R}^n$

$$\mathbf{x}(t) = [T(\xi_1, t), T(\xi_2, t), ..., T(\xi_n, t)]'$$
(7)

PBF systems are equipped with a variety of actuation and sensing hardware, which governs the form of $u(\bar{\xi},t)$ of Eq. (6) and the in situ measurements, respectively. Appendix A details the actuation and sensing modes considered in this paper. Broadly speaking, we consider actuation modes that implement combinations of inputs 1–5 of Fig. 1, labeled actuation modes A1–A4, and measurement modes that implement combinations of measurements 1–3 of Fig. 1, labeled measurement modes M1–M3.

3 Powder Bed Fusion Thermal Model

This section derives the models in Eqs. (1) and (2) from the heat flux balance of Eq. (6) and the actuator and measurement structure from Appendices A.1 and A.2, respectively. Our objective is to construct models for which the controllability and observability tools of Sec. 2.1 are applicable.

3.1 Powder Bed Fusion Model Assumptions and Construction. We first apply several simplifying assumptions to produce models amenable to controllability and observability analysis:

Assumption 1. $q_{\rm conv.}$ and $q_{\rm rad.}$ are assumed to be zero, because the Biot number for PBF is approximately Bi = 0.01 [28].

Assumption 2. Conduction into the unfused powder is negligible, as the loosely packed powder has a conductivity 100x smaller than the fused material [29]. This sets up a Neumann boundary condition at surfaces Γ , $\nabla T \cdot \hat{\mathbf{n}} = 0 \forall \mathbf{v} \in \Gamma$, as shown in Fig. 3(a), where $\nabla = (\frac{\partial}{\partial x}, \frac{\partial}{\partial y}, \frac{\partial}{\partial z})$, is the vector dot product, and $\hat{\mathbf{n}}$ is the direction normal to the domain Γ .

Assumption 3. Surfaces Λ have constant temperature T_0 , constructing the Dirichlet boundary condition $T = T_0 \, \forall v \in \Lambda$ and t (Fig. 3(a)). The PBF base plate and surrounding machine have a thermal mass that is typically orders of magnitude greater than the

part being built. Therefore, as do other researchers [30,31], we assume that the machine base plate is an ideal heat sink, and thus has constant temperature.

Assumption 4. We assume that new material added to the part in the timescale of analysis is negligible in comparison to the volume of V. For example, adding a $40\,\mu\mathrm{m}$ layer to a progressing $5\,\mathrm{mm}\times 10\,\mathrm{mm}\times 5\,\mathrm{mm}$ brick-shaped build constitutes only a 2% change in volume. Therefore, we treat the volume V as constant, with thermal properties equivalent to the bulk thermal properties. While this assumption excludes the initial stages of building and extreme long-term time scales from our analysis, it allows us to assess controllability and observability of systems with a fixed domain, which is common in control theory literature [17,18]. We anticipate results pertaining to a fixed V being foundational for analyzing systems with a dynamic V.

Assumption 5. We assume $q_{\rm phase}=0$. Capturing phase change requires nonlinear, often discontinuous switched, models that are not congruent with established observer and controller synthesis paradigms [32]. Neglecting $q_{\rm phase}$ induces error, but is commonly done in PBF modeling [22,25,26], and this assumption keeps our model tractable for controls analysis.

3.2 Reduction of Powder Bed Fusion Dynamics Through Finite Element Method. Assumptions 1–4 and 5 reduce Eq. (6) to the well-known conductive heat transfer boundary value problem defined by Fourier's Law

$$\frac{\partial T}{\partial t} = \frac{\kappa}{c\rho} \nabla^2 T \,\forall \, \xi \in V$$

$$T = T_0 \,\forall \, \xi \in \Lambda$$

$$\nabla T \cdot \hat{\mathbf{n}} = 0 \,\forall \, \xi \in \Gamma$$

$$\nabla T \cdot \hat{\mathbf{n}} = u(\bar{\xi}, t) \,\forall \, \bar{\xi} \in \Omega$$
(8)

 κ is the material thermal conductivity, and $\hat{\bf n}$ is defined in Assumption 2. Equation (8) does not have a closed-form solution for the arbitrarily complex problem domain and boundary conditions of PBF-manufactured parts. As explained before, we choose FEM to approximate the solution to Eq. (8) after discretizing V into a set of nodes and elements (Fig. 3(b)). According to Assumption 4, the nodes are assumed to hold fixed positions, which produces the system of ordinary differential equations in Eq. (9). We encourage interested readers to consult [33] for details on this process. $\mathbf{x}(t)$ in Eq. (9) contains the temperature states at all FEM nodes not on Λ , since these nodes on Λ are constrained to have the value T_0 . In Eq. (9), **K** captures the conductivity between adjacent nodes, M captures the thermal capacitance of each element, and the *load vector* function $\mathbf{R}(t)$ imposes the boundary conditions at the nodes on S. M and K are guaranteed to be symmetric and positive definite (PD) [33]. A PD M ensures that M^{-1} always exists. To ease the computational burden of inverting M, we elect to use a *lumped mass approximation*, which yields a diagonal PD M [34]

$$\dot{\mathbf{x}}(t) = -\mathbf{M}^{-1}\mathbf{K}\mathbf{x}(t) + \mathbf{M}^{-1}\mathbf{R}(t, u)$$
(9)

Equation (9) is the basis for the nonlinear PBF model, Eq. (10)

$$\dot{\mathbf{x}}(t) = \mathbf{A}\mathbf{x}(t) + \mathbf{r}(t, u)$$

$$\mathbf{y}(t) = \mathbf{g}(t, \mathbf{x}(t))$$
(10)

where $\mathbf{A} = -\mathbf{M}^{-1}\mathbf{K}$, $\mathbf{r}(t,u) = \mathbf{M}^{-1}\mathbf{R}(t,u)$, and $\mathbf{g}(t,\mathbf{x}(t))$ constructs the measurement. The structures of $\mathbf{r}(t,u)$ and $\mathbf{g}(t,\mathbf{x}(t))$ are based on the actuation and measurement modes of Appendix A. We now state some properties of A.

Remark 1. M and K are symmetric and PD; therefore, A is Hurwitz [35].

Table 1 Linear PBF thermal models

Case	Actuation	Measurement	State equations
A1M1	A1	M1	$\dot{\mathbf{x}}(t) = \mathbf{A}\mathbf{x}(t) + \mathbf{B}\mathbf{u}(t)$ $\mathbf{y}(t) = \mathbf{C}\mathbf{x}(t)$
A1M2	A1	M2	$\dot{\mathbf{x}}(t) = \mathbf{A}\mathbf{x}(t) + \mathbf{B}\mathbf{u}(t)$ $\mathbf{y}(t) = \mathbf{C}(t)\mathbf{x}(t)$
A2M1	A2	M1	$\dot{\mathbf{x}}(t) = \mathbf{A}\mathbf{x}(t) + \mathbf{B}(t)\mathbf{u}(t)$ $\mathbf{y}(t) = \mathbf{C}\mathbf{x}(t)$
A3M1	A3	M1	$\dot{\mathbf{x}}(t) = \mathbf{A}\mathbf{x}(t) + \mathbf{B}(t)\mathbf{u}(t)$ $\mathbf{y}(t) = \mathbf{C}\mathbf{x}(t)$
A2M2	A2	M2	$\dot{\mathbf{x}}(t) = \mathbf{A}\mathbf{x}(t) + \mathbf{B}(t)\mathbf{u}(t)$ $\mathbf{y}(t) = \mathbf{C}(t)\mathbf{x}(t)$
A3M2	A3	M2	$\dot{\mathbf{x}}(t) = \mathbf{A}\mathbf{x}(t) + \mathbf{B}(t)\mathbf{u}(t)$ $\mathbf{y}(t) = \mathbf{C}(t)\mathbf{x}(t)$

Theorem 1. Equation (10) is asymptotically stable, detectable, and stabilizable.

Proof. The stability, detectability, and stabilizability of Eq. (10) follow directly from $\mathbf{A} = -\mathbf{M}^{-1}\mathbf{K}$ being Hurwitz (Remark 1). \blacksquare THEOREM 2. A has real, negative eigenvalues and is always diagonalizable. Furthermore, all $[\mathbf{A}]_{ii} \neq 0$, $[\mathbf{A}]_{ij} \neq 0 \leftrightarrow \mathbf{A}_{ji} \neq 0$, and $[\mathbf{A}]_{ij} = 0 \leftrightarrow \mathbf{A}_{ji} = 0$.

Proof. A having real, negative eigenvalues, and being diagonalizable is a direct consequence of the facts that $\mathbf{M} = \operatorname{diag}([\mathbf{M}]_{11},...,[\mathbf{M}]_{nn})$ is PD, $\mathbf{K} = \mathbf{K}'$ is PD, and $\mathbf{A} = -\mathbf{M}^{-1}\mathbf{K}$ (Corollary 7.6.2 of Ref. [36]). Since \mathbf{M} is PD, all $[\mathbf{M}]_{ii} > 0$, and therefore, all $[\mathbf{M}^{-1}]_{ii} > 0$. Similarly, since \mathbf{K} is PD, all $[\mathbf{K}]_{ii} > 0$ [37]. Since $[\mathbf{A}]_{ij} = -[\mathbf{M}^{-1}]_{ii}[\mathbf{K}]_{ij}$ and $[\mathbf{K}]_{ij} \neq 0 \leftrightarrow [\mathbf{K}]_{ji} \neq 0$, all $[\mathbf{A}]_{ii} \neq 0$, $[\mathbf{A}]_{ji} \neq 0 \leftrightarrow [\mathbf{A}]_{ji} \neq 0$, and $[\mathbf{A}]_{ij} = 0 \leftrightarrow [\mathbf{A}]_{ji} = 0$.

3.3 Linear System Construction. Appendix B details how the actuation and measurement modes of Appendix A are used to linearize (10). Table 1 summarizes the results. Generally speaking, measurement mode **M2** and actuation modes **A2-A3** produce LTV system descriptions. As discussed in Appendix B, actuation mode **A4** and measurement mode **M3** produce uncontrollable and unobservable systems, respectively (Remarks 5 and 7), and are not used in these constructions. Case A1M1 is the only LTI system and all other cases are LTV in $\mathbf{B}(t)$ and/or $\mathbf{C}(t)$.

Figure 4 shows a representative set of A, B, and C matrices, corresponding to case A1M1 and the geometry of Figs. 7(a) and 7(b), which shows the typical sparseness of case A1M1. A is mostly comprised of zero entries because each node has only a small number of neighbors, and B and C are comprised mostly of zero entries because most nodes are not on Ω .

4 Controllability and Observability

In this section, we derive controllability and observability conditions for PBF models having a V without disconnected structures, meaning that all regions of V are connected by solid material, using the graph theory principles of Sec. 2.2. Equivalently, a continuous path may be constructed from the edges of $G(\mathbf{A}, \mathbf{B}, \mathbf{C})$ between any two nodes in the mesh of V.

4.1 Classical Controllability and Observability

Theorem 3. Given Case AIM1, and V without disconnected structures, the system is controllable and observable in the sense of Sec. 2.1 if A has all distinct eigenvalues and at least one node exists on Ω at all times.

Proof. Let $\delta(\lambda_i)$ denote the algebraic multiplicity of an eigenvalue of A, λ_i , defined as the number of times λ_i is repeated in the spectrum of A, spec(A). Let N_D be the minimum number of driver nodes (Sec. 2) needed to control the system in the sense of Sec. 2.1. Since A of case, A1M1 is always diagonalizable

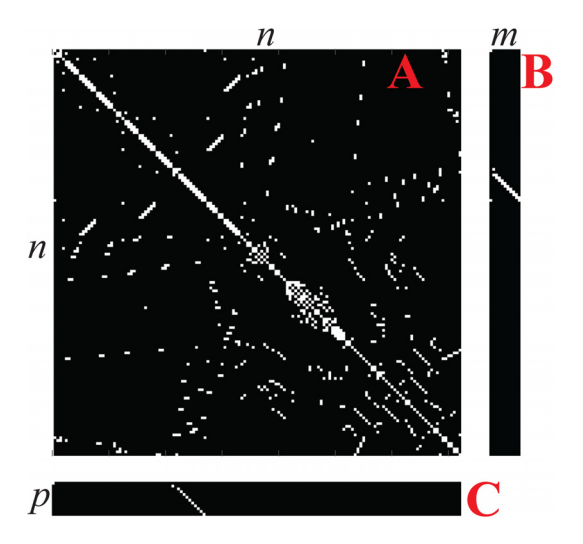


Fig. 4 $A \in \mathbb{R}^{n \times n}$, $B \in \mathbb{R}^{n \times m}$, and $C \in \mathbb{R}^{p \times n}$ matrix patterns, corresponding to the system shown in Figs. 7(a) and 7(b). Nonzero elements are shown in white, and zero elements are shown in black. For this system, n = 144, m = 11, and p = 12.

(Theorem 2), $N_D = \max_i \{\delta(\lambda_i)\}$ [38]. If the eigenvalues of **A** are all distinct, then $N_D = 1$. The only nodes in the mesh of V that are eligible to be driver nodes are those on Ω . By construction of V, at least one node exists on Ω . Furthermore, it follows from the proof in Ref. [38] that increasing N_D beyond the minimum value, $N_D > 1$, does not result in a loss of controllability. Therefore, if any subset of nodes on Ω is selected as driver nodes, the system is controllable. The claim for controllability is proven. Finally, the supplementary material of Ref. [38] shows that the minimum number of observer nodes, N_O , is the same as N_D ; having all-distinct eigenvalues of **A** implies an observable case A1M1.

In practice, Theorem 3 states that PBF systems that are (a) subjected to an arbitrary heat flux on Ω , and (b) equipped with an IR camera that measures Ω to arbitrary resolution (case A1M1), may always have their internal temperatures be controlled via the heat input and may always have these temperatures be estimated from the available measurements.

Remark 2. Having placed conditions for which case A1M1 is controllable/observable from a single node on Ω , we now place a crucial limitation on this result: If the system is not controllable or observable in the sense of Sec. 2.1 from a single node, then we cannot necessarily restore controllability or observability by adding more heat sources or by expanding the set of nodes visible to the PBF sensors. This would constitute adding more driver or observer nodes to exposed face Ω . Reference [38] shows that driver nodes in a network must be placed where the matrix $(\lambda^M \mathbf{I}_n - \mathbf{A})$ loses rank, where λ^M is the eigenvalue with maximal $\delta(\lambda_i) = \delta^M$. There is no guarantee that these $N_D > 1$ required driver nodes all lay on Ω if $\delta^M > 1$, and if they do not, then controllability or observability of case A1M1 is not possible.

Observability properties extend to cases A2M1 and A3M1, and controllability properties extend to case A1M2:

Corollary 1. Given cases A2M1 and A3M1, and V without disconnected structures, the systems are observable in the sense of Sec. 2.1 if A has all distinct eigenvalues and at least one node exists on Ω at all times. Case A1M2 is controllable under these same conditions.

Proof. Cases A1M1, and cases A2M1 and A3M1, have the same homogeneous dynamics and LTI output equations. Therefore, their observability properties are the same. Similarly, case A1M2 has the same controllability properties as case A1M1.

We now verify the observability of cases A1M2, A2M2, and A3M2.

THEOREM 4. If V contains no disconnected structures, there is at least one node in the camera field of view (FOV) at all times, and

A has all-distinct eigenvalues, then cases A1M2, A2M2, and A3M2 are observable.

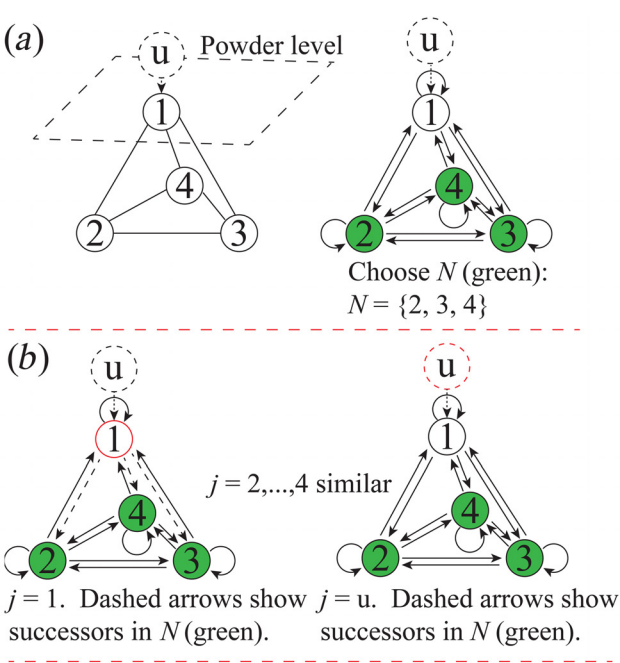
Proof. As explained in Remark 6, cases A1M2, A2M2, and A3M2 switch between a sequence of systems that resemble case A1M1 in their output equations. If *V* contains no disconnected structures, **A** has all-distinct eigenvalues and there is at least one node in the camera FOV at all times, each system in this sequence is observable by Theorem 3. It follows from Remark 0.3.2.i of Ref. [39] that cases A1M2, A2M2, and A3M2 are observable.

Remark 3. Theorem 3, Corollary 1, and Theorem 4 provide sufficient observability conditions for every case of Table 1.

4.2 Strong Structural Controllability/Observability. Having provided sufficient conditions for controllability and observability, we now assess the existence of systems that pass and fail these conditions. We phrase these results in terms of case A1M1, because Corollary 1 and Theorem 4 extend Case A1M1 observability results to other cases.

Theorem 5. It is possible to construct an instance of case A1M1 that is controllable and observable. It is possible to construct instances of cases A2M1 and A3M1 that are observable.

Proof. From Theorem 2, we know that all $[A_{ii}] \neq 0$. Therefore, it follows directly from Ref. [40] that case A1M1 is structurally



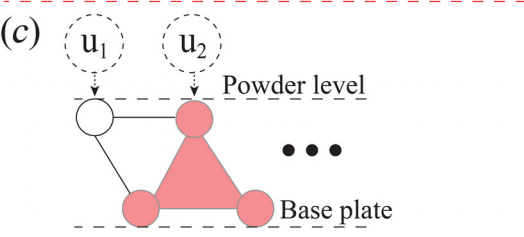


Fig. 5 Demonstration that the criterion of Theorem 6 is not satisfied for PBF models: (a) single element mesh for a 3D part domain V constructed according to case A1M1 and sample set N of noninput nodes. "u" denotes the input node. Observer nodes are suppressed for clarity. (b) Demonstration that no node j exists such that exactly one successor of j is contained in N. (c) Cross-sectional view of G(A, B, C) corresponding to a track of material having nonzero contact area with the base plate.

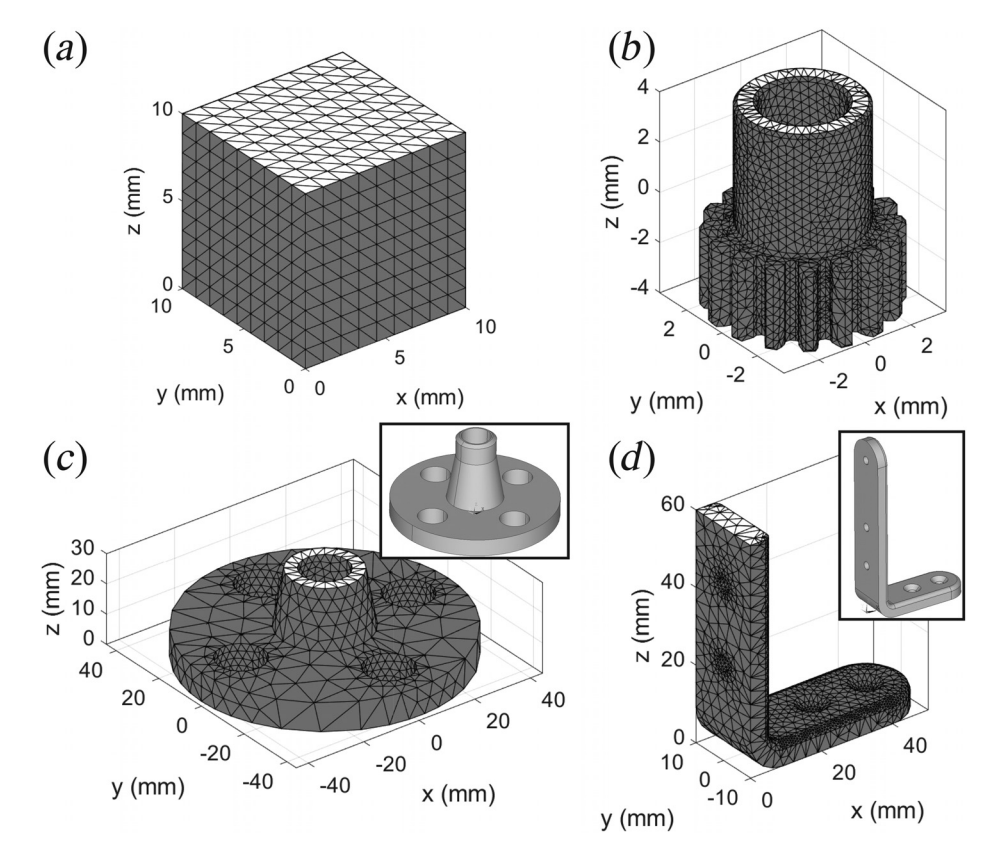


Fig. 6 Controllability and observability of simple part geometries: controllability and observability are determined with the eigenvalue check of Theorem 3. All four geometries satisfy this criterion. White-shaded faces denote Ω , which is the face visible to the measurement modes. (a) A simple cube. (b) McMaster-Carr part 7880K11. (c) McMaster-Carr part 44685K211. The inset denotes the full part geometry. (d) McMaster-Carr part 15655A41. The inset denotes the full part geometry.

controllable and observable, meaning that it is possible to construct an instance of case A1M1 that satisfies the sufficient condition of Theorem 3. Similarly, it is possible to construct instances of cases A2M1 and A3M1 that satisfy the sufficient condition of Corollary 1.

To assess if there are instances of case A1M1 that are not controllable and observable, we turn to the concepts of SSC and SSO, as given in Definition 1. We first approach the problem of SSC using the language of Ref. [41].

THEOREM 6. Restated from Ref. [41] for clarity: An LTI system described by the graph $G(\mathbf{A}, \mathbf{B}, \mathbf{C})$ (Sec. 2.2) is SSC if and only if the following holds: For every nonempty subset N of noninput nodes in the graph, there exists a node j in the graph (including input nodes), such that N contains exactly one successor of j. Given nodes w and v in $G(\mathbf{A}, \mathbf{B}, \mathbf{C})$, w is a successor of v if $G(\mathbf{A}, \mathbf{B}, \mathbf{C})$ contains a directed edge from v to w.

THEOREM 7. For a V having nonzero contact area with the base plate, it is impossible for case A1M1 to be SSC or SSO.

Proof. Figure 5(a) shows the graph corresponding to a simple 3D FEM mesh with only one node on Ω . Since the two criteria of Theorem 6 must hold for all subsets of N noninput nodes, we choose the N shown in Fig. 5(a). We check the validity of Theorem 6 as shown in Fig. 5(b). It is clear that varying our choice of j has two outcomes: There are three successors of j in N if j is chosen among the noninput nodes of the graph, or there are no successors of j in N if j is chosen to be the input node. The criterion of Theorem 6 is not satisfied; the instance of case A1M1 is not SSC.

As shown in Fig. 5(c), any FEM mesh for part domains that have nonzero contact area with the base plate will contain elements of this structure and/or elements that are entirely beneath Ω .

For there to be nonzero surface area in contact with the base plate, at least one element must have an entire face beneath Ω , leaving at most one node on Ω . Therefore, it is guaranteed that the criterion of Theorem 6 is not satisfied for case A1M1 generated from any V with nonzero contact area with the base plate, since the node set of Fig. 5(a) must always be present. Case A1M1 cannot be SSC. The proof for SSO proceeds similarly, because the question of controllability of G(A, B, C) is equivalent to the question of observability of G(A', B', C') [42].

Remark 4. The (strong) structural observability bounds of Theorems 5 and 7 extend to cases A2M1 and A3M1 by Corollary 1, and to cases A1M2, A2M2, and A3M2 by Theorem 4. This bounds the sufficient observability conditions of Remark 3 for all cases. Similarly, the (strong) structural controllability bounds of Theorems 5 and 7 extend to case A1M2 by Corollary 1.

Qualitatively, Remark 4 means that there exist part geometries for which accurately estimating the internal temperature field using data from either measurement mode M1 or M2 is impossible. However, there is at least one geometry where the estimation is possible. Furthermore, Remark 4 shows that geometries exist for which sculpting this temperature field in time via actuation mode A1 is also impossible, but that at least one geometry exists for which doing so is possible.

4.3 Case Study: Controllability and Observability of Sample Geometries. Figure 6 demonstrates how Theorem 3 is applied. The FEM meshes corresponding to four representative parts are displayed, and the faces containing nodes on Ω are shown in white. To remind the reader that these models apply to parts midway through building, the geometries of Figs. 6(c)

and 6(d) are sectioned along the z-axis. All four geometries produce A matrices with all-distinct eigenvalues. For all geometries of Fig. 6, this means the system is controllable and observable because at least one node exists on the measured face. We have yet to identify a geometry that produces a model with repeated eigenvalues, but Theorem 7 guarantees at least one exists. However, the size of Ω relative to V is small for Figs. 6(b)–6(d) relative to Fig. 6(a). Although temperature field control and estimation is possible for all four geometries, we expect doing so to become increasingly difficult as Ω shrinks. We justify this expectation in Sec. 5 by demonstrating how the "difficulty" of observation varies based on part and sensor configuration.

5 Energy Metric for Observation

Affirming observability is a binary metric and conveys no information regarding the relative difficulty of observation. Through examples, this section compares the energy absorption requirement of the sensors when observing different $T(\xi,t)$, as quantified by Eq. (11) [43]. $E_{\rm obs}$ of Eq. (11) is called the *observability energy*

$$E_{\text{obs}} = \sum_{k=0}^{K} ||\mathbf{y}[k]||_{2}^{2} = \mathbf{x}'[K]\mathbf{W}_{o}\mathbf{x}[K]$$
 (11)

Here, \mathbf{W}_o is the discrete time analog to Eq. (5), and the notation [k] denotes time $k\Delta t$, where Δt is the discrete time-step. Our procedure for converting from continuous to discrete time is given in the Supplemental Material on the ASME Digital Collection. Our case studies assess $E_{\rm obs}$ for the cases in Table 1. For LTI measurement modes (cases A1M1, A2M1, and A3M1), we compute \mathbf{W}_o for different quantities of sensors, and assess $E_{\rm obs}$ as a function of several temperature states $\mathbf{x}[K]$. For cases A1M2, A2M2, and

A3M2, E_{obs} is computed by summing all $||\mathbf{y}[k]||_2^2$. This is done because computing \mathbf{W}_o is impractical for cases A1M2, A2M2, and A3M2, and Eq. (11) shows that the two methods are equivalent for cases A1M1, A2M1, and A3M1.

We compute $E_{\rm obs}$ for the two 2D geometries shown in Fig. 7, discretized with the displayed FEM meshes. These meshes use midside nodes which are not visualized for clarity except when stated otherwise. As will be explained, for both geometries and LTI measurement modes (cases A1M1, A2M1, and A3M1), we test how $E_{\rm obs}$ changes under two conditions: (1) holding the temperature T fixed within an expanding radius of nodes while keeping the observed nodes constant (Figs. 7(a) and 7(c)), and holding the temperature field fixed while expanding the number of observed nodes (Figs. 7(b) and 7(d)). For LTV measurement modes, we consider only case A3M2, and test how $E_{\rm obs}$ changes as a function of expanding observed nodes for fixed scan parameters (Table 2), which are as follows: Constant P[k] = 27.5 W, constant $(r_b)^2[k] = 0.15$ mm², starting from $x_c[0] = 0$ and moving with constant velocity v = 8 mm/s. These simulations are discretized with $\Delta t = 0.5$ ms and run for K = 1152 time steps. The operating point of actuation mode A3 is $[P_0, r_{b,0}^2] = [27.5, 0.11]$. The output matrices, C[k], are constructed by selecting nodes within the moving camera FOV.

5.1 Energy Metric Results. We first illustrate trends in $E_{\rm obs}$ for time-invariant observations (cases A1M1, A2M1, and A3M1) of 2D PBF models. Figure 7 demonstrates this test, which examines $E_{\rm obs}$ under two conditions: first, fix the number of sensors, observing the highlighted nodes, while varying $\mathbf{x}[K]$ of Eq. (11), and second, fix $\mathbf{x}[K]$ while varying the number of sensors. We construct a varying $\mathbf{x}[K]$ as follows: All nodes of Fig. 7 enclosed by a black semicircle have a constant temperature T=1, with all other nodes having T=0 (ambient temperature in the chosen

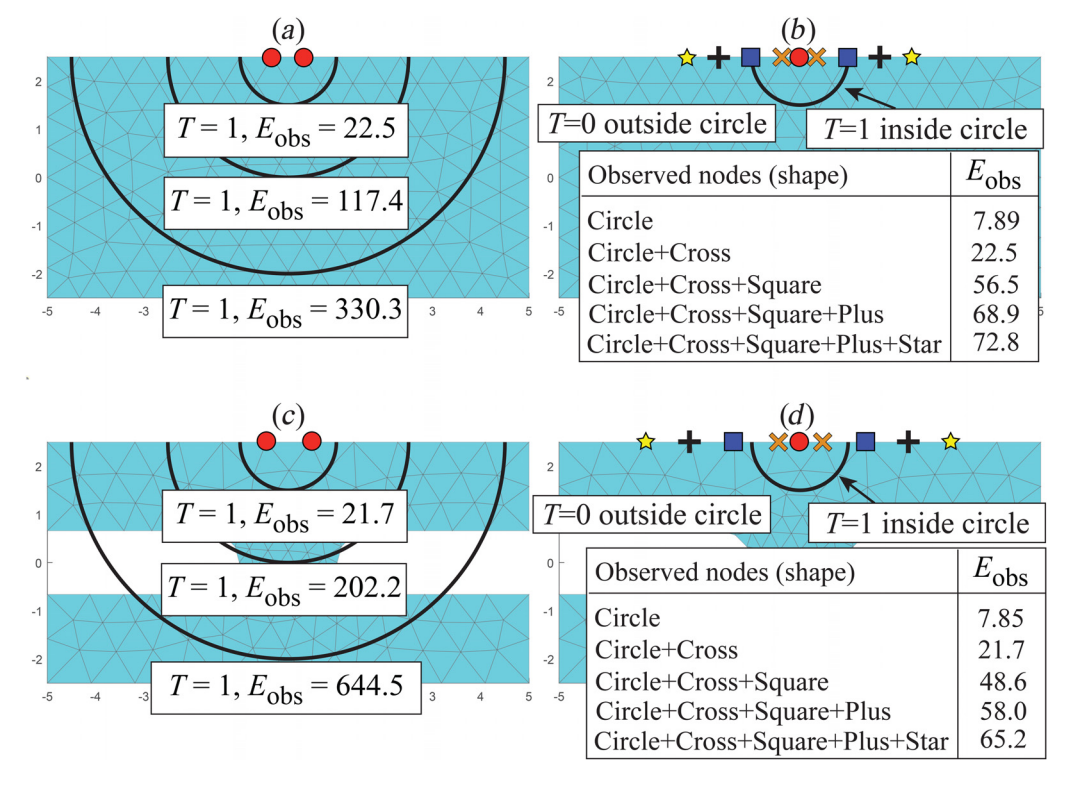


Fig. 7 $E_{\rm obs}$ associated with given x[K]. Midside nodes were excluded for clarity, with the exception of the circles in subplots (b) and (d). Sensors for both geometries are observing the highlighted nodes on Ω . x[K] is defined by maintaining all nodes within regions enclosed by black semicircles at T=1 and leaving nonenclosed nodes at T=0. (a), (c): effect of changing x[K] on $E_{\rm obs}$ for a fixed sensor configuration (observed nodes in red). (b), (d): effect of changing the number of sensors on $E_{\rm obs}$ for fixed x[K], and fixed sensor locations.

Table 2 Observation energy of cases A1M2 and A3M2

	Geometry	Geometry of Fig. 7(a)		Geometry of Fig. 7(c)	
N closest nodes to $x_c(t_k)$ observed	$E_{ m obs}$	$E_{ m obs}/N$	$E_{ m obs}$	$E_{ m obs}/N$	
$ \begin{array}{c} N = 1 \\ N = 3 \end{array} $	2.77×10^9 5.96×10^9	2.77×10^9 1.99×10^9	8.27×10^9 1.74×10^{10}	8.27×10^9 5.80×10^9	
N=5 $N=5$	6.48×10^9	1.39×10^{9} 1.30×10^{9}	1.83×10^{10}	3.66×10^9	

units). We observe in Figs. 7(a) and 7(c) that as the radius of enclosed nodes increases, so too does $E_{\rm obs}$. This is intuitive: Observing ${\bf x}$ from measurements of ${\bf \Omega}$ requires absorbing increasing energy as the components of ${\bf x}$ beneath ${\bf \Omega}$ grow more energetic, as measured by the growth of $||{\bf x}[K]||_2^2$ relative to a constant $||{\bf y}[K]||_2^2$. Part geometry plays a role in this information flow. The I-beam geometry of Fig. 7(c) cannot conduct heat from the interior to ${\bf \Omega}$, and thus to the sensors, as efficiently as the rectangular-shaped geometry of Fig. 7(a). Accordingly, $E_{\rm obs}$ increases faster as the enclosed node radius increases in Fig. 7(c) than in Fig. 7(a).

Figures 7(b) and 7(d) demonstrate the effect of changing the number of sensors has on $E_{\rm obs}$. We construct a fixed $\mathbf{x}[K]$, and the number of nodes within the sensor FOV is varied. We observe that in both geometries, as the number of observed nodes increases, so too does $E_{\rm obs}$. This result is intuitive because the amount of energy absorbed by the sensors will naturally increase as the sensors image more of Ω . As Figs. 7(b) and 7(d) show, $E_{\rm obs}$ continues to increase even when nodes outside the circle of elevated temperature (which have T=0) are included in the observation. $E_{\rm obs}$ increases despite the additional sensors recording the value 0 because recording this measurement still requires expending energy.

We next illustrate trends in E_{obs} for time-varying observations (case A3M2) of 2D PBF models, using the time discretization of the Supplemental Material on the ASME Digital Collection. Using the given laser parameters, we calculate a sequence of system states $\{\mathbf{x}[k]\}_{k=0}^{1152}$ for both geometries of Fig. 7. The action of $\mathbf{C}_d[k]$ at each time-step is implemented by selecting each $\mathbf{y}[k]$ in the output signal $\{\mathbf{y}[k]\}_{k=0}^{1152}$ to be the temperature of the N nodes closest to the laser center, $x_c(t_k)$, at time-step k. Table 2 demonstrates these results for several values of N. Changing N represents observing the PBF melt pool with a sensor with a varying FOV. These values are higher than those reported in Fig. 7 due to the PBF laser producing higher temperatures, and thus output signals, than setting T=1 arbitrarily. The reader should not compare $E_{\rm obs}$ between the LTI and LTV cases. We notice the same trend observed in the previous section: as the measurement FOV widens (N increases), so too does E_{obs} , for the same reason as before. Additionally, Table 2 shows that the energy absorbed per sensor, $E_{\rm obs}/N$, decreases as N increases. We draw two conclusions: (1) that using a large number of sensors (large N) does not substantially improve the observation quality, relative to smaller N, as measured by a diminishing growth in E_{obs} , and (2) as N increases, each sensor absorbs less energy when observing $\mathbf{x}|k|$.

6 Conclusions

This paper represents a foundational exploration into the controllability and observability of the internal temperature fields of parts being manufactured via the PBF process, for eventual quality control and temperature control application. It is shown that a FEM-based discretization of the governing PBF physics produces a model that is unconditionally asymptotically stable, stabilizable, and detectable. We investigate six PBF hardware architectures within the framework of linear systems analysis. These architectures include industry-standard and emerging PBF hardware,

therefore, we expect our investigation to accommodate future industry trends. We show that having all-distinct eigenvalues is sufficient for controllability and observability of linearized (LTI) models (cases A1M1 and A1M2), and for observability of all six examined cases. This shows that accurately estimating the internal temperature field from a FEM-based model is possible for certain part geometries, constructed from a variety of PBF hardware configurations. Assessing controllability and observability of more advanced sensor configurations like embedded thermal sensors [44,45] is a direction of future research. These configurations add new boundary conditions to PBF thermal physics and change the measurement dimension over time, and thus go beyond the assumptions in this work.

Furthermore, we present an initial characterization of the relative energy demands of observing these linearized systems, to better understand the practicality of state observation. These procedures let us quantify the change in estimator performance as we alter the available sensors. These are important considerations for the controls engineer, who must distinguish between the binary metric of observability, and consequences of the energetic requirements for state observation. For example, we show that increasing the number of sensors cannot necessarily restore observability to a deficient system. However, for a system that is observable, adding sensors lowers the energetic burden at each sensor when observing the state. There are diminishing returns to adding more sensors, suggesting that the high resolution camera data that is currently being used [46,47] provides orders of magnitude more data than is required for accurate process estimation [16]; the authors have performed detailed investigations on state observation effectiveness with decreasing camera resolution [48].

Acknowledgment

The authors acknowledge technical support from ANSYS and professor Prasad Mokashi at the Ohio State University for his assistance with FEM theory.

Funding Data

- Air Force Research Laboratory (C.N. RX9-OSU-20-5-AFRL2; Funder ID: 10.13039/100006602).
- The Smart Vehicle Concepts Center, a Phase III National Science Foundation Industry-University Cooperative Research Center (Grant No. NSF IIP 1738723; Funder ID: 10.13039/100000001).

Appendix A: Powder Bed Fusion Actuation and Measurement Modes

A.1 Actuation (A) Modes. Powder bed fusion systems are currently actuated, or proposed to be actuated, via four different modes. Each of these modes governs the form of $u(\bar{\xi},t)$ incident on the part. Different actuation modes are not typically applied simultaneously, although some researchers have proposed systems that permit the simultaneous application of different modes [49,50].

(A1) $u(\bar{\xi},t)$ as an arbitrary function. Actuation mode A1 is applicable to an electron beam (e-beam) system (E-PBF) operating such that the heat flux on Ω can be prescribed and spatiotemporally graded [51,52], as shown in input 1 (Fig. 1(a)). In E-PBF, the raster speed (order of 10^4 mm/s [53]) meets the critical speed for heat input across successive rasters to outpace heat loss due to conduction [54], which allows us to approximate $u(\bar{\xi},t)$ as arbitrary. A laser PBF (L-PBF) system that uses a digital light processing filter to distribute laser flux can also produce an arbitrary heat flux function across Ω [49,50].

 $(A2)\ u(\bar{\xi},t)$ as a Gaussian function with inputs 2–5. Incident laser or e-beam flux is assumed to have a Gaussian-distributed intensity [31,55], and a total of M heat sources (spots) are assumed active

$$u(\bar{\xi},t) = \sum_{i=1}^{M} \frac{P_i}{r_{b,i}^2} \exp\left(-\frac{(x_{c,i} - x_{\bar{\xi}})^2 + (y_{c,i} - y_{\bar{\xi}})^2}{r_{b,i}^2}\right)$$
(A1)

Here, $x_{\bar{\xi}}$ and $y_{\bar{\xi}}$ denote the x and y coordinates of the point $\bar{\xi}$, respectively. The system provides complete control authority over inputs 2–5 in Fig. 1(*b*): (1) laser or e-beam effective power, $P_i(t)$; (2) laser or e-beam radius, $r_{b,i}(t)$; and (3) and (4) laser or e-beam centroid, $x_{c,i}(t)$ and $y_{c,i}(t)$. Actuation mode A2 is applicable to L-PBF with single- (M=1) and multi- (M>1) laser configurations, and E-PBF operating such that the raster speed is, at most, on the same order as the effective time constant of the thermal system.

(A3) $u(\xi,t)$ as in A2, but without Inputs 4–5. A3 represents the minimal control fidelity envisioned, and is the current state of the art [56–58]. The laser or e-beam centroids of Eq. (A1) are not control variables; instead the centroids $x_{c,i}(t)$ and $y_{c,i}(t)$ proceed on a schedule of G-code commands.

 $(A4)\ u(\bar{\xi},t)$ proceeds along a predetermined trajectory. This is the current open loop actuation method used by almost all PBF machines. $u(\bar{\xi},t)$ remains arbitrary because its trajectory cannot be altered in real time.

A.2 Measurement (M) Modes. Powder bed fusion temperature is currently measured, or proposed to be measured, via three different modes, or combinations thereof.

(M1) Fixed field of view thermal camera. The camera has a FOV on Ω to collect emitted infrared light from the part [59], $y = h(\bar{x}, \bar{y}, \alpha, \beta) T(\bar{\xi}, t)$. $h(\bar{x}, \bar{y}, \alpha, \beta)$ models the action of an infrared camera with an $\alpha \times \beta$ -pixel FOV centered at the point (\bar{x}, \bar{y}) . h maps the temperature field on Ω , $T(\bar{\xi}, t)$, to a measured temperature at each pixel in the camera FOV. We do not yet specify this mapping, which includes camera mechanics and pixel spacing, and thus describe h as a generic windowing function. In cases where the measurement is a single point (spot) pyrometer centered at (\bar{x}, \bar{y}) [60], the windowing function is given by $h(\bar{x}, \bar{y}, 1, 1)$. Measurement mode **M1** is possible for both E-PBF and L-PBF systems (measurement 1, Fig. 1). (M2) Source-centered field of view thermal camera. Emitted infrared light from face Ω passes through the galvonometer mirrors (Fig. 1(b)) before being split off to a set of sensors. For multilaser configurations as in actuation mode A2, each light path may be equipped with an infrared (IR) camera. For a sensor array of M cameras, [61], the FOV is coaxial with the laser centroids, and $y = (\sum_{i=1}^{M} h(x_{c,i} + \bar{x}_i, y_{c,i} + \bar{y}_i, \alpha_i, \beta_i))T(\bar{\xi}, t); h$ is defined as in measurement mode M1, and \bar{x}_i and \bar{y}_i capture an offset between the laser centroid and the center of a camera FOV. If these sensors are single point pyrometers [62] or a pyrometer array [63], the windowing function is given by $h(x_{c,i} + \bar{x}_i, y_{c,i} + \bar{y}_i, 1, 1)$. Measurement mode **M2** is only possible with L-PBF (measurement 2, Fig. 1(b)).

(M3) Environmental temperature measurement, T₀, via a thermocouple embedded in the base plate. This is the most basic

temperature measurement available (measurement 3, Fig. 1). This sensor is used for real-time environmental temperature feedback and is commonly available in commercial PBF systems. We model this measurement as $y = h(\bar{x}, \bar{y}, 1, 1)T(\underline{\xi}, t)$, where h is the (single pixel FOV) generic windowing function of measurement mode M1, and $T(\underline{\xi}, t)$ within a region $(\bar{x} \pm \epsilon, \bar{y} \pm \epsilon)$ is the temperature on surfaces Λ .

Appendix B: Constructing Linear Input/Output Expressions

B.1 Expression of $\mathbf{r}(t,u)$ for Each Actuation Mode. $\mathbf{r}(t,u)$ has a different form for each actuation mode (Appendix A.1), thus influencing the controllability of the process. Each of the following subsections derives the form of $\mathbf{r}(t,u)$ for a given form of the input $u(\bar{\xi},t)$.

B.1.1 Actuation Mode A1. Actuation mode A1 assumes that the form of $u(\bar{\xi}, t)$ is arbitrary. This input structure allows for a convenient simplification of the FEM-derived $\mathbf{r}(t, u)$, [33]

$$\mathbf{r}(t,u) = \mathbf{M}^{-1}\mathbf{R}(t,u) = \mathbf{M}^{-1}\sum_{e}\int_{S_{e}}u(\xi,t)\mathbf{N}'_{e}dS_{e}$$
 (B1)

where \mathbf{N}_e are shape functions that interpolate the value of $T(\xi,t)$ from the temperatures at the nodes that bound the e^{th} element. S_e is the boundary of the e^{th} element. $u(\xi,t)=u(\bar{\xi},t)$ if $\xi\in\Omega$ and $u(\xi,t)=0$ otherwise. Details are in the Supplemental Material on the ASME Digital Collection. After simplification, the PBF input is

$$\mathbf{r}(t,u) \approx \mathbf{B}\mathbf{u}(t)$$
 (B2)

B.1.2 Actuation Mode A2. Under actuation modes A2 and A3, $u(\bar{\xi},t)$ assumes the Gaussian form specified in Eq. (A1). Therefore, Eq. (B1) may be expanded into the form shown in Eq. (B3). Actuation mode A2 assumes that $P_i(t) \geq 0$, $r_{b,i}^2(t) > 0$, and $x_{c,i}(t)$, and $y_{c,i}(t)$ are freely controllable at each instant of time t for all M lasers in the system, constructing the input $\mathbf{u}_1(t)$ of Eq. (B4)

$$\mathbf{r}(t, \mathbf{u}_1(t)) = \mathbf{M}^{-1} \sum_{e \in \Omega} \int_{S_e} \sum_{i=1}^{M} \frac{P_i(t)}{r_{b,i}^2(t)} e^{-\frac{\Delta v_i(t)^2 + \Delta y_i(t)^2}{r_{b,i}^2(t)}} \mathbf{N}_e' dS_e$$
 (B3)

$$\mathbf{u}_{1}(t) = [P_{1}(t), r_{b,1}^{2}(t), x_{c,1}(t), y_{c,1}(t), \dots P_{M}(t), r_{b,M}^{2}(t), x_{c,M}(t), y_{c,M}(t)]'$$
(B4)

In Eq. (B3), $\Delta x_i(t) = x_{c,i}(t) - x\bar{\xi}$, and $\Delta y_i(t) = y_{c,i}(t) - y\bar{\xi}$, for $\bar{\xi} = \xi \in \Omega$ and time-dependent laser centerpoint coordinates $x_{c,i}(t)$ and $y_{c,i}(t)$.

Under these conditions, the integrand of Eq. (B3) is continuously differentiable with respect to all components of $\mathbf{u}(t)$; therefore, we use Leibniz's integration rule to linearize Eq. (B3) about the time-varying operating point $\mathbf{u}_0(t) = (P_{0,i}(t), r_{b0,i}(t), x_{c0,i}(t), y_{c0,i}(t))$. By linearizing Eq. (B3), we control first-order deviations from $\mathbf{u}_0(t)$. The linearization procedure yields

$$\mathbf{r}(t, \mathbf{u}_{1}(t)) \approx \mathbf{r}(t, \mathbf{u}_{0}(t)) + \mathbf{B}(t)\delta\mathbf{u}_{1}(t)$$

$$\delta\mathbf{u}_{1}(t) = [\delta P_{1}(t), \, \delta r_{b,1}^{2}(t), \, \delta x_{c,1}(t), \, \delta y_{c,1}(t), \dots$$

$$\delta P_{M}(t), \, \delta r_{b,M}^{2}(t), \, \delta x_{c,M}(t), \, \delta y_{c,M}(t)]'$$

$$\mathbf{u}_{1}(t) = \mathbf{u}_{0}(t) + \delta\mathbf{u}_{1}(t)$$

where $\mathbf{B}(t)$ is

$$\begin{split} \mathbf{B}(t) = \mathbf{M}^{-1} \left[\frac{\partial \mathbf{r}}{\partial P_{1}}, \frac{\partial \mathbf{r}}{\partial r_{b,1}^{2}}, \frac{\partial \mathbf{r}}{\partial x_{c,1}}, \frac{\partial \mathbf{r}}{\partial y_{c,1}}, \dots, \frac{\partial \mathbf{r}}{\partial P_{M}}, \frac{\partial \mathbf{r}}{\partial r_{b,M}^{2}}, \frac{\partial \mathbf{r}}{\partial x_{c,M}}, \frac{\partial \mathbf{r}}{\partial y_{c,M}} \right] \Big|_{\mathbf{u}_{0}(t)} \\ \left[\dots, \frac{\partial \mathbf{r}}{\partial P_{i}}, \frac{\partial \mathbf{r}}{\partial r_{b,i}^{2}}, \frac{\partial \mathbf{r}}{\partial x_{c,i}}, \frac{\partial \mathbf{r}}{\partial y_{c,i}}, \dots \right] \Big|_{\mathbf{u}_{0}(t)} \end{split}$$

$$=\begin{bmatrix} \vdots \\ \left(\sum_{e} \int_{S_{e}} \frac{1}{r_{b0,i}^{2}(t)} \exp(-\sigma_{0,i}(t)) \mathbf{N}_{e} dS\right)' \\ \left(\sum_{e} \int_{S_{e}} \frac{P_{0,i}(t) \exp(-\sigma_{0,i}(t))}{\left(r_{b0,i}^{2}(t)\right)^{2}} (-1 + \sigma_{0,i}(t)) \mathbf{N}_{e} dS\right)' \\ \left(\sum_{e} \int_{S_{e}} -\frac{2P_{0,i}(t)}{\left(r_{b0,i}^{2}(t)\right)^{2}} \Delta x_{0,i}(t) \sigma_{0,i}(t) \exp(-\sigma_{0,i}(t)) \mathbf{N}_{e} dS\right)' \\ \left(\sum_{e} \int_{S_{e}} -\frac{2P_{0,i}(t)}{\left(r_{b0,i}^{2}(t)\right)^{2}} \Delta y_{0,i}(t) \sigma_{0,i}(t) \exp(-\sigma_{0,i}(t)) \mathbf{N}_{e} dS\right)' \\ \vdots \\ \sigma_{0,i}(t) = \frac{\Delta x_{0,i}(t)^{2} + \Delta y_{0,i}(t)^{2}}{r_{b0,i}^{2}} \end{bmatrix}$$

From Eqs. (B3) and (B5), we observe that $P_{0,i}(t)(\frac{\partial \mathbf{r}}{\partial P_i}|_{\mathbf{u}_0(t)}) = \mathbf{r}(t,\mathbf{u}_0(t))$. Therefore, we express $\mathbf{r}(t,\mathbf{u}_0(t))$ in terms of $\mathbf{B}(t)$ as $\mathbf{r}(t,\mathbf{u}_0(t)) = \mathbf{B}(t)[P_{0,1}(t),0,...,P_{0,2}(t),0,...,P_{0,M}(t),0,...]'$. This allows us to express $\mathbf{r}(t,\mathbf{u}_1(t))$ as

$$\mathbf{r}(t, \mathbf{u}_1(t)) = \mathbf{B}(t)(\delta \mathbf{u}_1(t) + [P_{0,1}(t), 0, ..., P_{0,2}(t), 0, ..., P_{0,M}(t), 0]')$$

Within the context of linear systems, the input $\delta \mathbf{u}_1(t)$ is a free choice, therefore we construct the control input $\delta \mathbf{u}_1(t) = \mathbf{u}(t) - [P_{0,1}(t), 0, ..., P_{0,2}(t), 0, ..., P_{0,M}(t), 0, ...]'$. This cancels the influence of the operating point to form the input relationship $\mathbf{B}(t)\mathbf{u}(t)$, where $\mathbf{u}(t) = [P_1(t), \delta r_{b,1}^2, \delta x_{c,1}, \delta y_{c,1}, ..., P_M(t), \delta r_{b,M}^2, \delta x_{c,M}, \delta y_{c,M}]'$.

B.1.3 Actuation Mode A3. As in actuation mode A2, in actuation mode A3, $\mathbf{r}(t,u)$ assumes the form given in Eq. (B3). However, under actuation mode A3 only $P_i(t) \geq 0$ and $r_{b,i}^2(t) > 0$ are available control inputs. Therefore, $\mathbf{u}_1(t) = [P_1(t), r_{b,1}^2(t), \ldots, P_M(t), r_{b,M}^2(t)]'$. The laser centroids $(x_{c,i}(t), y_{c,i}(t))$ are treated as time-varying parameters instead of control inputs. Linearization of Eq. (B3) under these conditions proceeds similarly to Appendix B.1.2. The resulting construction $\mathbf{B}(t)$ is defined similarly to Eq. (B5). Now, $\mathbf{B}(t)$ only consists of partial derivaties $\frac{\partial \mathbf{r}}{\partial P_i}$ and $\frac{\partial \mathbf{r}}{\partial r_{i,j}^2}$ for $i=1,\ldots,M$.

B.1.4 Actuation Mode A4. We suppose $\mathbf{r}(t,u(t))$ has two components: a component from the predetermined input, $u(\bar{\boldsymbol{\xi}},t)$, which we denote as $\mathbf{r}(t,u(\bar{\boldsymbol{\xi}},t))=\mathbf{r}(t)$, and a component from any hypothetical freely adjustable input, $\bar{\mathbf{u}}(t)$. Since the system cannot be influenced by any $\bar{\mathbf{u}}(t)$, we have the construction

$$\mathbf{r}(t, u(t)) = \mathbf{0}\bar{\mathbf{u}}(t) + \mathbf{r}(t) \tag{B6}$$

Remark 5. By the criteria of Sec. 2.1, actuation mode A4 produces a trivially rank deficient controllability Gramian, therefore, PBF using actuation mode A4 is uncontrollable [18], and thus we do not consider it in our analysis.

B.2 Expression of $\mathbf{g}(t, \mathbf{x})$ for Each Measurement Mode. Eq. (10), has a different form for each measurement mode, thus influencing the observability of the process. Each of the following subsections derives the form of $\mathbf{g}(t, \mathbf{x}(t))$, for a given windowing function h.

B.2.1 Measurement Mode M1. Under measurement mode **M1**, the available measurement is a camera or set of spot pyrometers having a fixed FOV. Therefore, the output of the system $\mathbf{y}(t) = \mathbf{g}(t, \mathbf{x}(t)) \in \mathbb{R}^p$ is defined as

$$\mathbf{y}(t) \equiv \mathbf{C}\mathbf{x}(t) \tag{B7}$$

where $\mathbf{C} \in \mathbb{R}^{p \times n}$ selects all nodes on Ω that lay in the fixed FOV of the camera, or fixed FOV of the set of cameras. If state component $[\mathbf{x}]_j$ is visible in the FOV, an output component $[\mathbf{y}]_i$ is associated with it by setting $[\mathbf{C}]_{ij} = 1$. All other elements of \mathbf{C} are zero. In the case where the measurements are spot measurements from a set of pyrometers centered at $(\bar{x}_i, \bar{y}_i, z = \bar{z})$, \mathbf{C} selects the set of nodes on Ω that are closest to each $(\bar{x}_i, \bar{y}_i, z = \bar{z})$.

B.2.2 Measurement Mode M2. Under measurement mode M2, the available measurements are cameras that have light paths that are coaxial with the lasers, thus their FOVs move with the laser centerpoints. Each laser centerpoint is treated as a governing parameter of $\mathbf{y}(t)$. Therefore, the system output, $\mathbf{y}(t) = \mathbf{g}(t, \mathbf{x}(t)) \in \mathbb{R}^p$, is defined as

$$\mathbf{y}(t) \equiv \mathbf{C}(t)\mathbf{x}(t) \tag{B8}$$

Here, $\mathbf{C}(t) \in \mathbb{R}^{p \times n}$ is a time-varying selection matrix that selects the set of nodes on Ω being observed by the moving melt pool camera FOVs.

Remark 6. Although the lasers move continuously, the cameras are discrete instruments. They return a sequence of measurements $\{y[0],y[1],\ldots\}$, spaced by the sample rate, Δt . We reconstruct a continuous y(t) via a sample-and-hold procedure: Between each sample time, $k\Delta t$, the camera positions are treated as fixed. The relationship y(t) = C(t)x(t) becomes $y(t) = C(\zeta_k)x(t)$, where ζ_k represents the nodes in the camera FOVs during the k^{th} measuring interval. For notational convenience, we abbreviate $C(\zeta_k)$ as C(t).

B.2.3 Measurement Mode M3. Under measurement mode M3, the only available temperature measurement is a spot measurement at the base plate. Under Assumption 3, Λ presents an isothermal boundary condition. The measurement y(t) takes the constant value $y(t) = T_0 \ \forall \ t \geq 0$, regardless of any temperature field in V, $\mathbf{x}(t)$. Therefore, no meaningful information regarding $\mathbf{x}(t)$ is captured by these measurements. Accordingly, under measurement mode M3, $y(t) = \mathbf{g}(t, \mathbf{x}(t))$ may be expressed as $y(t) = \mathbf{0}\mathbf{x}(t)$.

Remark 7. By the criteria of Sec. 2.1, measurement mode M3 produces a trivially rank deficient observability Gramian, therefore, PBF using only M3 is unobservable [18]. Thus, we do not include it in our analysis.

References

(B5)

- [1] Bhavar, V., Kattire, P., Patil, V., Khot, S., Gujar, K., and Snigh, R., 2017, Additive Manufacturing Handbook, Vol. 15, CRC Press, pp. 251–261.
- [2] Wang, T., Zhu, Y. Y., Zhang, S. Q., Tang, H. B., and Wang, H. M., 2015, "Grain Morphology Evolution Behavior of Titanium Alloy Components During Laser Melting Deposition Additive Manufacturing," J. Alloys Compd., 632, pp. 505–513.
- [3] Wood, N., Schwalbach, E., Gillman, A., and Hoelzle, D., May 2021, "The Ensemble Kalman Filter as a Tool for Estimating Temperatures in the Powder Bed Fusion Process," American Control Conference, New Orleans, LA, May 25–28, pp. 4369–4375.
- [4] Ridwan, S., Mireles, J., Gaytan, S., Espalin, D., and Wicker, R., 2014, "Automatic Layerwise Acquisition of Thermal and Geometric Data of the Electron Beam Melting Process Using Infrared Thermography," Proceedings of the Annual International Solid Freeform Fabrication Symposium, pp. 343–352.
- [5] Peng, H., Ghasri-Khouzani, M., Gong, S., Attardo, R., Ostiguy, P., Gatrell, B. A., Budzinski, J., Tomonto, C., Neidig, J., Shankar, M. R., Billo, R., Go, D. B., and Hoelzle, D., 2018, "Fast Prediction of Thermal Distortion in Metal Powder

- Bed Fusion Additive Manufacturing: Part 1, a Thermal Circuit Network Model," Addit. Manuf., 22, pp. 852-868.
- [6] Peng, H., Ghasri-Khouzani, M., Gong, S., Attardo, R., Ostiguy, P., Rogge, R. B., Aboud Gatrell, B., Budzinski, J., Tomonto, C., Neidig, J., Shankar, M. R., Billo, R., Go, D. B., and Hoelzle, D. J., 2018, "Fast Prediction of Thermal Distortion in Metal Powder Bed Fusion Additive Manufacturing: Part 2, a Quasi-Static Thermo-Mechanical Model," Addit. Manuf., 22, pp. 869–882.
 [7] Gokuldoss, P. K., Kolla, S., and Eckert, J., 2017, "Additive Manufacturing
- Processes: Selective Laser Melting, Electron Beam Melting and Binder Jetting Selection Guidelines," Mater. (Basel), 10(6), p. 672.
- [8] DebRoy, T., Wei, H., Zuback, J., Mukherjee, T., Elmer, J., Milewski, J., Beese, A., Wilson-Heid, A., De, A., and Zhang, W., 2018, "Additive Manufacturing of Metallic Components-Process, Structure and Properties," Prog. Mater. Sci., 92, pp. 112–224.
- [9] Wei, H., Elmer, J., and DebRoy, T., 2016, "Origin of Grain Orientation During Solidification of an Aluminum Alloy," Acta Mater., 115, pp. 123–131.
 [10] Mower, T., and Long, M., 2016, "Mechanical Behavior of Additive Manufac-
- tured, Powder-Bed Laser-Fused Materials," Mater. Sci. Eng. A, 651, pp. 198-213.
- [11] Yadollahi, A., Shamsaei, N., Thompson, S., and Seely, D., 2015, "Effects of Process Time Interval and Heat Treatment on the Mechanical and Microstructural Properties of Direct Laser Deposited 316l Stainless Steel," Mater. Sci. Eng. A, 644, pp. 171–183.
- [12] Yeung, H., Lane, B., Donmez, M., Fox, J., and Neira, J., 2018, "Implementation of Advanced Laser Control Strategies for Powder Bed Fusion Systems," Procedia Manuf., 26, pp. 871-879.
- [13] Arisoy, Y., Criales, L., Ozel, T., Lane, B., Moylan, S., and Donmez, A., 2017, "Influence of Scan Strategy and Process Parameters on Microstructure and Its Optimization in Additively Manufactured Nickel Alloy 625 Via Laser Powder Bed Fusion," Int. J. Adv. Manuf. Technol., 90(5–8), pp. 1393–1417.
- [14] Khairallah, S., Anderson, A., Rubenchik, A., and King, W., 2016, "Laser Powder-Bed Fusion Additive Manufacturing: Physics of Complex Melt Flow and Formation Mechanisms of Pores, Spatter, and Denudation Zones," Acta Mater., 108, pp. 36-45.
- [15] Pellegrino, J., May 2013, "Measurement Science Roadmap for Metal-Based Additive Manufacturing," Energetics, Inc. for National Institute of Standards and Technology, Gaithersburg, MD, Report.
- [16] Gaikwad, A., Yayari, R., Montazeri, M., Cole, K., Bian, L., and Rao, P., 2020. "Toward the Digital Twin of Additive Manufacturing: Integrating Thermal Simulations, Sensing, and Analytics to Detect Process Faults," IISE Trans., **52**(11), pp. 1204–1217.
- [17] Chen, C.-T., 1999, Linear System Theory and Design, 3rd ed., Oxford University Press, New York.
- [18] Antsaklis, P. J., and Michel, A. N., 2007, A Linear Systems Primer, Vol. 5, Birkhauser, Boston, MA, pp. 195-232.
- [19] Mayeda, H., and Yamada, T., 1979, "Strong Structural Controllability," SIAM J. Control Optim., 17(1), pp. 123–138.
- [20] Gracy, S., Garin, F., and Kibangou, A., 2017, "Strong Structural Input and State Observability of LTV Network Systems With Multiple Unknown Inputs," IFAC World Congress, Toulouse, France, pp. 7357-7362
- [21] Liu, Y., Slotine, J., and Barabasi, A., 2011, "Controllability of Complex Networks," Nature, 473(7346), pp. 167–173.
- [22] Yavari, M., Cole, K., and Rao, P., 2019, "Thermal Modeling in Metal Additive Manufacturing Using Graph Theory," ASME J. Manuf. Sci. Eng., 141(7), p. 071007.
- [23] Wang, D., and Chen, X., 2021, "Closed-Loop High-Fidelity Simulation Integrating Finite Element Modeling With Feedback Controls in Additive Manufacturing," ASME J. Dyn. Syst. Meas. Control, 143(2), p. 021006. [24] Ren, Y., Wang, Q., and Michaleris, P., 2021, "A Physics-Informed Two-Level
- Machine-Learning Model for Predicting Melt-Pool Size in Laser Powder Bed Fusion," ASME J. Dyn. Syst. Meas. Control, 143(12), p. 121006.
- [25] Schwalbach, E., Donegan, S., Chapman, M., Chaput, K., and Groeber, M., 2019, "A Discrete Source Model of Powder Bed Fusion Additive Manufacturing Thermal History," Addit. Manuf., 25, pp. 485-498.
- [26] Wolfer, A., Aires, J., Wheeler, K., Delplanque, J.-P., Rubenchik, A., Anderson, A., and Khairallah, S., 2019, "Fast Solution Strategy for Transient Heat Conduction for Arbitrary Scan Paths in Additive Manufacturing," Addit. Manuf., **30**, p. 100898.
- [27] Zhang, Y., Shapiro, V., and Witherell, P., August 2019, "Towards Thermal Simulation of Powder Bed Fusion on Path Level," ASME Paper No. DETC2019-98046.
- [28] Paul, R., Anand, S., and Gerner, F., 2014, "Effect of Thermal Deformation on Part Errors in Metal Powder Based Additive Manufacturing Processes," ASME J. Manuf. Sci. Eng., 136(3), p. 031009.
- [29] Rombouts, M., Froyen, L., Gusarov, A. V., Bentefour, E. H., and Glorieux, C., 2005, "Photopyroelectric Measurement of Thermal Conductivity of Metallic Powders," J. Appl. Phys., 97(2), p. 024905.
- [30] He, X., DebRoy, T., and Fuerschbach, P., 2003, "Probing Temperature During Laser Spot Welding From Vapor Composition and Modeling," J. Appl. Phys., 94(10), pp. 6949-6958.
- [31] Raghavan, A., Wei, H., Palmer, T., and DebRoy, T., 2013, "Heat Transfer and Fluid Flow in Additive Manufacturing," J. Laser Appl., 25(5), p. 052006.
- [32] Zakirov, A., Belousov, S., Bogdanova, M., Korneev, B., Stepanov, A., Perepelkina, A., Levchenko, V., Meshkov, A., and Potapkin, B., 2020, "Predictive Modeling of Laser and Electron Beam Powder Bed Fusion Additive Manufacturing of Metals at the Mesoscale," Addit. Manuf., 35, p. 101236.
- [33] Cook, R. D., Malkus, D. S., and Plesha, M. E., 1989, Concepts and Applications of Finite Element Analysis, 3rd ed., Wiley, New York.

- [34] ANSYS, 2017, ANSYS Mechanical APDL Theory Reference, release, 18.2 ed.,
- ANSYS, Canonsburg, PA.
 [35] Johnson, C. R., 1977, "The Inertia of a Product of Two Hermitian Matrices," J. Math. Anal. Appl., 57(1), pp. 85–90.
- [36] Horn, R., and Johnson, C., 2012, Matrix Analysis, 2nd ed., Cambridge University Press, New York, p. 486.
- [37] Johnson, C. R., 1970, "Positive Definite Matrices," Am. Math. Mon., 77(3), pp. 259-264.
- [38] Yuan, Z., Zhao, C., Di, Z., Wang, W., and Lai, Y., 2013, "Exact Controllability of Complex Networks," Nat. Commun., 4(1), p. 2447.
- [39] Petreczky, M., Tanwani, A., and Trenn, S., 2015, "Observability of Switched Systems," Hybrid Dynamical Systems: Observation and Linear Control (Lecture Notes in Control and Information Sciences), M. Djemai and M. Defoort, eds., Vol. 457, Springer, Heidelberg, Germany, pp. 205-240, Chap. 8.
- [40] Cowan, N., Erick, J., Vilhena, D., Freudenberg, J., and Bergstrom, C., 2012, Nodal Dynamics, Not Degree Distributions, Determine the Structural Controllability of Complex Networks," PLoS One, 7(6), p. e38398.
- [41] Reissig, G., Hartung, C., and Svaricek, F., 2014, "Strong Structural Controllability and Observability of Linear Time-Varying Systems," IEEE Trans. Autom. Control, 59(11), pp. 3087–3092.
- [42] Liu, Y., Slotine, J., and Barabasi, A., 2013, "Observability of Complex Systems," Proc. Natl. Acad. Sci. U. S. A., 110(7), pp. 2460–2465. [43] Pasqualetti, F., Zampieri, S., and Bullo, F., 2014, "Controllability Metrics, Lim-
- itations and Algorithms for Complex Networks," Trans. Control Network Syst., **1**(1), pp. 40–52.
- [44] Stoll, P., Mathew, J., Spierings, A., Bauer, T., Maier, R., and Wegener, K., 2016, "Embedding Fibre Optical Sensors Into SLM Parts," Solid Freeform Fabrication Symposium, Austin, TX, pp. 1815-1825.
- [45] Stoll, P., Leutenecker-Twelsiek, B., Spierings, A., Klahn, C., and Wegener, K., 2017, "Temperature Monitoring of an SLM Part With Embedded Sensor," Industrialized Additive Manufacturing - Proceedings of Additive Manufacturing in Products and Applications—AMPA2017, Zurich, Switzerland
- [46] Mohr, G., Altenburg, S., Ulbricht, A., Heinrich, P., Baum, D., Maierhofer, C., and Hilgenberg, K., 2020, "In-Situ Defect Detection in Laser Powder Bed Fusion by Using Thermography and Optical Tomography-Comparison to Computed Tomography," Metals, 10(1), p. 103.
- Yeung, H., Lane, B., and Fox, J., 2019, "Part Geometry and Conduction-Based Laser Power Control for Powder Bed Fusion Additive Manufacturing," Addit. Manuf., 30, p. 100844.
- [48] Wood, N., Schwalbach, E., Gillman, A., and Hoelzle, D., 2021, "On the Diminishing Returns of Thermal Camera Resolution for PBF Temperature Estimation," International Solid Freeform Fabrication Symposium, pp.
- [49] Roy, N., Behera, D., Dibua, O., Foong, C., and Cullinan, M., 2019, "A Novel Microscale Selective Laser Singering (µ-Sls) Process for the Fabrication of Microelectronic Parts," Microsyst. Nanoeng., 5(1), p. 64.
- [50] Roy, N. K., Behera, D., Dibua, O. G., Foong, C. S., and Cullinan, M. A., 2018, "Single Shot, Large Area Metal Sintering With Micrometer Level Resolution," Opt. Express, 26(20), pp. 25534–25544.
- [51] Rafi, H., Karthik, N., Haijun, G., Starr, T., and Stucker, B., 2013, "Microstructures and Mechanical Properties of ti6al4v Parts Fabricated by Selective Laser Melting and Electron Beam Melting," J. Mater. Eng. Perform., 22(12), pp. 3872-3883.
- [52] Antonysamy, A., Meye, J., and Prangnell, P., 2013, "Effect of Build Geometry on the β-Grain Structure and Texture in Additive Manufacture of Ti-6Al-4V by Selective Electron Beam Melting," Mater. Charact., 84, pp. 153-168.
- [53] Ramirez, D., Murr, L., Martinez, E., Hernandez, D., Martinez, J., Machado, B., Medina, F., Frigola, P., and Wicker, R., 2011, "Novel Precipitate-Microstructural Architecture Developed in the Fabrication of Solid Copper Components by Additive Manufacturing Using Electron Beam Melting," Acta Mater., 59(10), pp. 4088-4099.
- [54] Juechter, V., Scharowsky, T., Singer, R., and Körner, C., 2014, "Processing Window and Evaporation Phenomena for Ti-6Al-4V Produced by Selective Electron Beam Melting," Acta Mater., 76, pp. 252-258.
- [55] Yuan, P., and Gu, D., 2015, "Molten Pool Behaviour and Its Physical Mechanism During Selective Laser Melting of Tic/alsi10 mg Nanocomposites: Simulation and Experiments," J. Phys. D: Appl. Phys., 48(3),
- [56] Zhong, Q., Tian, X., Huang, X., Huo, C., and Li, D., 2021, "Using Feedback Control of Thermal History to Improve Quality Consistency of Parts Fabricated Via Large-Scale Powder Bed Fusion," Addit. Manuf., 42, p. 101986
- Wang, Q., Michaleris, P., Nassar, A. R., Irwin, J. E., Ren, Y., and Stutzman, C. B., 2020, "Model-Based Feedforward Control of Laser Powder Bed Fusion
- Additive Manufacturing," Addit. Manuf., 31, p. 100985.

 [58] Kruth, J., Mercelis, P., Van Vaerenbergh, J., and Craeghs, T., 2007, "Feedback Control of Selective Laser Melting," Third International Conference on Advanced Research in Virtual and Rapid Prototyping, pp. 521-527.
- [59] Rodriquez, E., Medina, F., Espalin, D., Terrazas, C., Muse, D., Henry, C., MacDonald, E., and Wicker, R. B., 2012, "Integration of a Thermal Imaging Feedback Control System in Electron Beam Melting," Proceedings of the
- Annual International Solid Freeform Fabrication Symposium, pp. 945–961.
 [60] Cola, M., and Betts, S., 2018, "In-Situ Process Mapping Using Thermal Quality SignaturesTM During Additive Manufacturing With

- Titanium Alloy Ti-6Al-4V," Sigma Labs, Santa Fe, NM, Report No. BY6-2018-003IR Rev0.

 [61] Clijsters, S., Craeghs, T., Buls, S., Kempen, K., and Kruth, J.-P., 2014, "In Situ Quality Control of the Selective Laser Melting Process Using a High-Speed, Real-Time Melt Pool Monitoring System," Int. J. Adv. Manuf. Technol., 75(5-8), pp. 1089–1101.
- [62] Chivel, Y., and Smurov, I., 2010, "On-Line Temperature Monitoring in Selective Laser Sintering/Melting," Phys. Procedia, 5(B), pp. 515–521.
- [63] Stockman, T., Knapp, C., Henderson, K., Carpenter, J., and Schneider, J., 2018, "Stainless Steel 304l Lens Am Process Monitoring Using In-Situ Pyrometer Data," JOM, 70(9), pp. 1835–1843.